Measurement of the Aerothermodynamic State in a High Enthalpy Plasma Wind-Tunnel Flow

Tobias Hermann[1], Stefan Löhle[2], Fabian Zander[3]

Universität Stuttgart, Institut für Raumfahrtsysteme, Pfaffenwaldring 29, D–70569 Stuttgart, Germany

Stefanos Fasoulas[4]

Universität Stuttgart, Institut für Raumfahrtsysteme, Pfaffenwaldring 29, D–70569 Stuttgart, Germany

Abstract

This paper presents spatially resolved measurements of absolute particle densities of N_2, N_2^+, N, O, N^+, O^+, e^- and excitation temperatures of electronic, rotational and vibrational modes of an air plasma free stream. All results are based on optical emission **spectroscopy** data. The measured parameters are combined to determine the local mass–specific enthalpy of the free stream. **The analysis of the radiative transport, relative and absolute intensities, and spectral shape is used to determine various thermochemical parameters.** The model uncertainty of each analysis method is assessed. **The plasma flow is shown to be close to equilibrium**. The strongest deviations from equilibrium occur for N, N^+ and N_2^+ number densities in the free stream. Additional measurements of the local mass-specific enthalpy are conducted using a mass injection probe **as well as** a heat flux and total pressure probe. The agreement between all methods of enthalpy determination is **good**.

---

[1]Postdoctoral Research Assistant, Hypersonics Group, Osney Thermofluids Laboratory.
[2]Research Scientist, Head of High Enthalpy Flow Diagnostic Group, IRS.
[3]Postdoctoral Researcher, High Enthalpy Flow Diagnostic Group, IRS.
[4]Professor, Director, IRS.

Nomenclature

A_{ul} = Einstein coefficient, s^{-1}

c = speed of light in vacuum, $m\,s^{-1}$

DoF = depth of field, mm

D = diameter, mm

h = Planck constant, $J\,s$

h_0 = **total mass–specific enthalpy, $MJ\,kg^{-1}$**

$h_{formation}$ = heat of formation, $MJ\,kg^{-1}$

K_M = proportionality constant for air, $N^{0.5}\,m^{0.5}\,s\,kg^{-1}$

L_λ = spectral radiance, $W\,m^{-2}\,nm^{-1}\,sr^{-1}$

k_B = **Boltzmann's constant, $J\,K^{-1}$**

M_∞ = free stream Mach number

n_j = number density of species j, m^{-3}

$n_{j,i}$ = population density of species j excited state i, m^{-3}

p = pressure, hPa

Q = partition function

u_∞ = free stream velocity, $m\,s^{-1}$

$\dot{q}$ = heat flux, $kW\,m^{-2}$

R = nose radius, mm

R = specific gas constant, $J\,kg^{-1}\,K^{-1}$

β = velocity gradient, s^{-1}

Δ = spatial width, mm

$\Delta\lambda$ = half width at half maximum line broadening, nm

Δz = **characteristic length scale for self-absorption, m**

ε_λ = spectral emission coefficient, $W\,m^{-3}\,nm^{-1}\,sr^{-1}$

γ = ratio of specific heats

λ = wavelength, nm

σ = **absorption cross section, m^2**

θ = characteristic temperature, K

ξ = mass fraction

Subscripts

EQ	=	equilibrium
el	=	electronic excitation
eff	=	effective
FC	=	flat faced cylinder
G	=	Gaussian
HS	=	hemisphere
L	=	Lorentzian
rot	=	rotational
tot	=	total
trans	=	translational
w	=	wall
vib	=	vibrational

1. Introduction

Interplanetary sample return missions require a re-entry maneuver into the Earth's atmosphere. The heat load experienced by the entering vehicle is very high due to the heating of air by the strong bow shock in front of the capsule [1, 2]. Therefore, heat shields are used to protect the sample. Plasma wind tunnel experiments are primarily conducted to validate and assess the performance of the heat shield materials [3, 4, 5, 6]. The wind tunnel facilities provide continuous high enthalpy flows which aim to replicate the aerothermodynamic environment of the post shock stagnation streamline [7]. The goal of such experiments is to simulate the stagnation point heat load by **replicating** the boundary layer **thermochemical state** [8]. However, energy insertion into the gas in the **plasma** generator differs greatly from the phenomena in a hypersonic shock. **In this study, a magnetoplasmadynamic arc-jet flow is investigated, where the energy transfer primarily occurs by heating the gas with an electric arc**. Hence, the question arises, how well the actual

3

post shock flowfield is replicated. Therefore, the free stream of a plasma wind

20 tunnel flow has to be characterized in detail [9, 10, 11, 12, 13, 14].

In this study the aerothermodynamic properties of the arc-jet plasma wind tunnel flow are related to a hypersonic post shock region. The chosen flow condition used to assess this matter is representative of the Hayabusa trajectory point at $78.8\,\mathrm{km}$ altitude. The re-entry trajectory point features a velocity

25 of $11.7\,\mathrm{km\,s^{-1}}$ and a free stream density of $1.91 \times 10^{-5}\,\mathrm{kg\,m^{-3}}$ [15]. The corresponding subsonic flow condition in the **plasma wind tunnel** has already been characterized by multiple diagnostic techniques including optical emission spectroscopy from the vacuum ultraviolet to the near infrared, heat flux and pressure probes, and Fabry-Perot-interferometry [16, 17, 18]. The current work presents

30 additional measurements and analysis methods that complement the existing data. The main focus is on the analysis and interpretation of the aerothermochemistry. As mass-specific enthalpy is arguably the most important parameter for the composition of such a flow, this value is the central focus of the study at hand. Therefore, different probe measurements and a spectroscopic approach

35 are used to deduce this parameter.

2. Plasma Wind Tunnel Experiments

This section **presents** the experiments carried out in the plasma wind tunnel PWK1. The facility consists of an evacuated test section and a magnetoplasmadynamic arc-jet generator. An electric arc is established between a central

40 cathode, located close to the nozzle throat, and a ring-shaped anode, located at the end of the nozzle [19, 20]. This design allows a steady electric arc between cathode and anode to be maintained with nitrogen gas passing through the arc. Oxygen is injected in a nozzle segment after the throat, in order to protect the cathode from **erosion** by oxidation. The heated gas expands through a noz-

45 zle and forms a free jet in the test section. Probes are exposed to the plasma flow which are mounted on a movable platform operated by a CNC stepping motor [7]. For the current condition the axial distance between the probe stag-
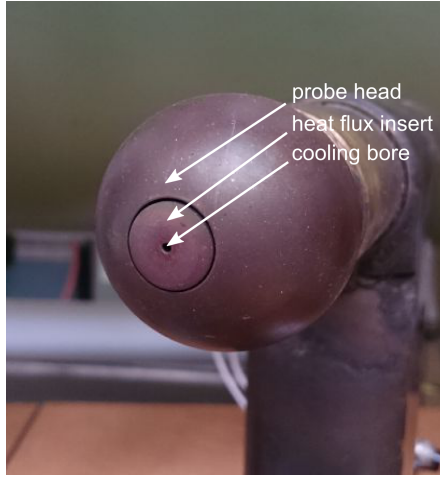
4

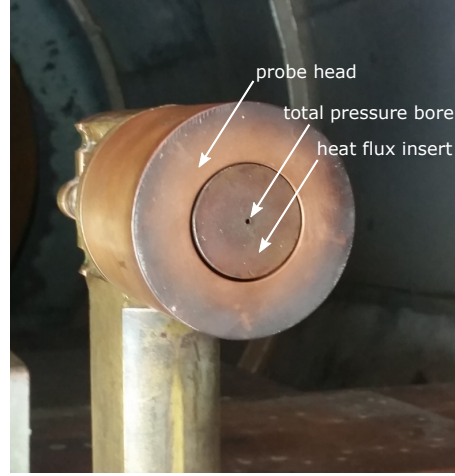Figure 1: Photograph of the **mass-injection** probe [21].

Figure 2: Photograph of the $\dot{q}$ and p_{tot} probe.

nation point and the nozzle exit is 270 mm. The condition is established using a static pressure of 1660 Pa in the test chamber, an air mass flow of $18\,\mathrm{g\,s^{-1}}$ and an arc current of 1220 A [16].

2.1. *Mass-injection* Probe

A photograph of the **mass-injection** probe is shown in Fig. 1. A detailed description of the probe and the underlying boundary layer theory is presented in [21]. The cylindrical probe has a diameter of 50 mm with a hemispherical head shape. A 14.5 mm diameter insert is used to determine the stagnation region heat flux. Here, the temperature rise of a known cooling water mass flow is used to determine the surface heat flux. A bore hole in the stagnation point is used to inject a small amount of nitrogen (in the **order** of several $\mathrm{mg\,s^{-1}}$) into the boundary layer. The resulting heat flux reduction is used to determine the local mass-specific enthalpy of the plasma flow stagnation streamline [22, 21].

2.2. Heat Flux and Total Pressure Probe

The second probe is used to measure the stagnation point heat flux and total pressure [23, 16]. A photograph of the flat faced 80 mm

5

diameter cylindrical probe is shown in Fig. 2. The 40 mm diameter insert is used to measure the heat flux, analogously to the enthalpy probe's insert, while the bore hole in the stagnation point is used to measure the total pressure. Local mass-specific enthalpy is determined from the probe data by applying the ASTM standard test method for the calculation of stagnation enthalpy from heat transfer and stagnation pressure for a hemispherical probe at low Mach numbers $(0.1 < M_\infty < 2)$ [24]

$$h_0 \approx h_0 - h_{\text{w}} = \frac{K_M \dot{q}}{\sqrt{p_{\text{tot}}/R_{\text{eff}}}} \left[\frac{(\beta D_{HS}/u_\infty)_{\text{mod. Newtonian}}}{(\beta D_{HS}/u_\infty)_{\text{subsonic}}} \right] \tag{1}$$

with the negligible wall enthalpy h_{w}, the constant for air $K_M = 2561 \, \text{N}^{0.5} \, \text{m}^{0.5} \, \text{s} \, \text{kg}^{-1}$, the stagnation point heat flux $\dot{q}$ and the effective radius R_{eff}. Note that this formulation is based on an approach developed by Zoby for hypersonic flows which has been extended to low Mach numbers [25]. The correction to the subsonic regime is conducted by considering the non–dimensional velocity gradients in front of a hemisphere for the modified Newtonian theory

$$(\beta D_{HS}/u_\infty)_{\text{mod. Newtonian}} = \left[\frac{4 \left[(\gamma - 1) M_\infty^2 + 2 \right]}{\gamma M_\infty^2} \right]^{0.5} \tag{2}$$

and in a subsonic environment

$$(\beta D_{HS}/u_\infty)_{\text{subsonic}} = 3 - 0.755 M_\infty^2 \quad (M_\infty < 1) \tag{3}$$

with the freestream velocity u_∞, the hemispherical diameter D_{HS} and, assuming a fully dissociated gas, the ratio of specific heats γ=1.13. **As the probe geometry in the present study is a flat faced cylinder, an equivalent hemisphere with radius R_{eff} has to be defined [26].** This reproduces the velocity gradient in front of the flat faced cylinder, specified by the radius R. For this purpose, the work of Brown is used which applies potential flow theory to subsonic arc-heated flows [27]. Here, the Mach number dependence of the non-dimensional velocity gradients for hemispheres and flat faced cylinders are compiled. For the present case, a free stream Mach number of $M_\infty = 0.97$ is determined from the velocity measurements of Zander et al. [17] and the results presented in section 3. This results in the ratio $(\beta D/u_\infty)_{HS}/(\beta D/u_\infty)_{FC} = 2.63$

6

between a hemisphere (HS) and a flat faced cylinder (FC) of equal diameter.
In order to create the same velocity gradient β for both geometries the radii have to obey

$$\frac{\beta R_{\text{eff}}/u_\infty}{\beta R/u_\infty} = \frac{R_{\text{eff}}}{R} = 2.63 \qquad (4)$$

with the free stream velocity u_∞. The resulting effective radius is then used in Eq. (1) to obtain the local mass-specific enthalpy of the stagnation streamline.

2.3. Optical Emission Spectroscopy

In this study, two different optical setups are used to acquire spectral data **from** the Ultraviolet (UV) to the NIR. **Measurements using the two systems are taken in separate tests and are subsequently merged to form a single data set. Axially resolved measurements along the x-axis are conducted using system A, shown in Fig. 3, and radially resolved measurements along the z-axis are conducted with system B, shown in Fig. 4 [16]. Axially resolved measurements with system A are taken on the centre line ($z = 0$). Radially resolved measurements with system B are taken at six axial locations ($x = 210; 235; 250; 260; 265; 268\,\text{mm}$).** Both focusing optics are used with the same Acton SpectraPro 2758 spectrograph in Czerny-Turner configuration. A detailed description of the spectroscopic setup and the calibration procedure is given in [16]. Both optical systems have identical properties. The relevant system parameters are compiled in Table 1.

Both datasets of the two optical systems are combined to yield a spatially resolved emission field. **To match the spatial resolution of the system A measurement an interpolation of the system B measurements is conducted. The radial profile of the measured radiation is linearly interpolated between the six distinct axial locations. This is conducted for each wavelength at each axial location measured with system A.** These interpolated profiles are then Abel-transformed using the f-interpolation type algorithm of Fulge et al. [28] yielding local emission coefficients assum-
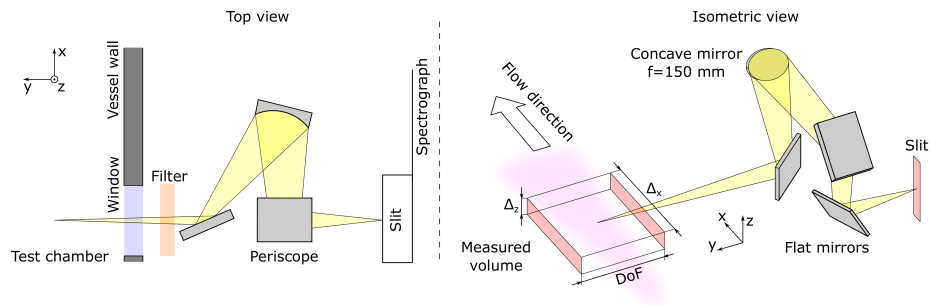
7

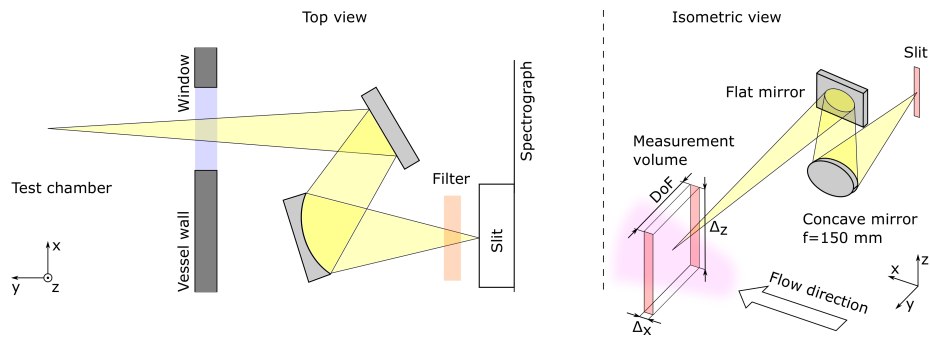Figure 3: Optical setup A for the axially resolved emission spectroscopic measurements.

Figure 4: Optical setup B for the radially resolved emission spectroscopic measurements.

Table 1: Properties of the optical emission spectroscopic setup [16].

Parameter	Value
Wavelength range / nm	300–1000
Spectral resolution / $\mathrm{nm\,px^{-1}}$	0.12
Instrumental broadening $\Delta\lambda_\mathrm{L}$; $\Delta\lambda_\mathrm{G}$ / nm	0.12; 0.24
Grating / $\mathrm{g\,mm^{-1}}$	300
Slit width / μm	80
Magnification	0.11
F-Number	6
DoF / mm	89
Spatial resolution (x) / $\mathrm{mm\,px^{-1}}$	0.23
Spatial broadening Δ_G (x) / mm	0.6
Measurement volume Δ_x; Δ_z [a] / mm	59; 1.6

[a] Vice versa for the system shown in Fig. 4.

ing rotational symmetry. **The** calculated emission coefficients are subsequently scaled in such a way that their spatial integral corresponds to the spectral radiance measured with system A. This procedure results in a spectrally resolved three-dimensional emission field. **However**, only the stagnation streamline is considered for further analysis.

In addition to the UV-NIR measurements, spectroscopic measurements in the Vacuum Ultraviolet (VUV) are used for the analysis of the current study. The VUV radiation has previously been analyzed and is compiled in [16, 6].
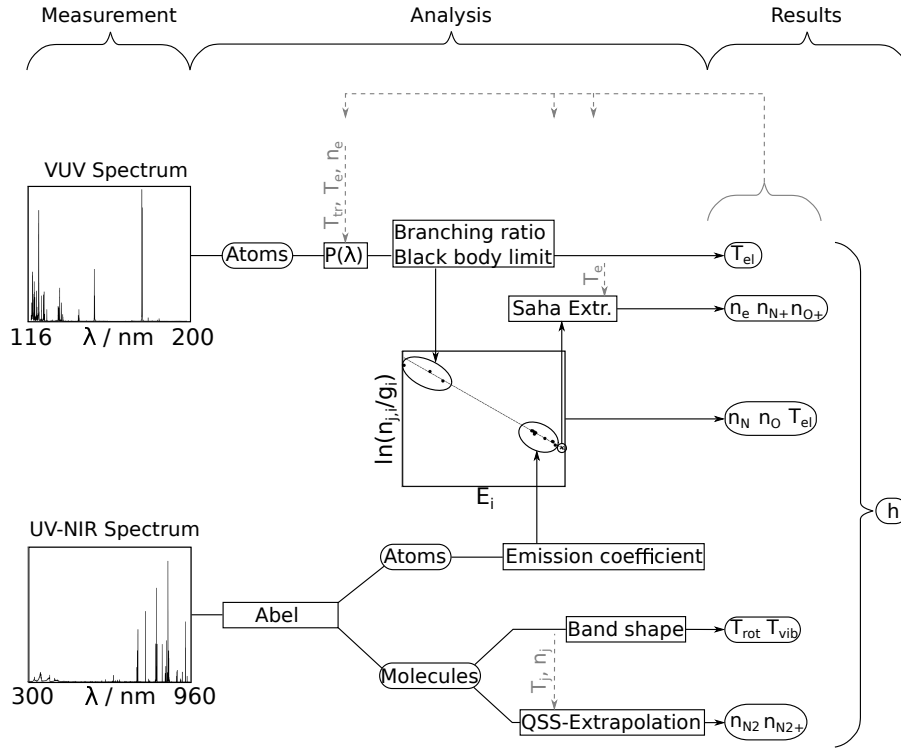
Figure 5: Schematic of the analysis procedure.

2.4. Analysis Methods for Emission Spectroscopy

This section presents the analysis methods that are used to deduce thermo-dynamic parameters from the measured spectra. Detailed discussions of most methods are presented in [16, 29]. An overview of the overall methodology is shown in Fig. 5. Some methods require input parameters that are obtained through other methods. Therefore, the complete analysis is conducted itera-tively until each method converges. In the following, a brief description of each method is given.

2.4.1. High Energy Atomic Population Densities - Emission Coefficient (EC)

The absolute emitted radiation of optically thin atomic transitions in the NIR is used to infer the upper state population density of the respective tran-

10

sition $n_{j,u}$ via

$$\varepsilon = \frac{n_{j,u} A_{ul} hc}{4\pi\lambda_0}$$ (5)

with the energy difference of the transition hc/λ_0 and the Einstein coefficient A_{ul} [30, 31, 16]. **The assumptions of optically thin lines was validated by calculating the radiative transport of each line along the optical path** of the spectroscopic system. **Lower state population densities of the investigated lines are estimated by evaluating the best Boltzmann-fit at the respective energy level. All NIR transitions exhibited negligible self-absorption and are thus optically thin.**

2.4.2. Low Energy Atomic Population Densities - Branching Ratio (BR)

The characteristic shape of self absorbing atomic multiplets in the VUV is used to deduce the lower state population density of the respective transition [32, 33, 34]. This is conducted by performing a simulation of the radiative transport where the lower state number density of each transition is varied until the best agreement between simulation and experiment is achieved. Here, the spatial distribution of highly excited states is used for the spatial distribution of low energy states [16, 29].

2.4.3. Low Energy Atomic Population Densities -Black Body Limit Extrapolation (BBL)

Low energy population densities are determined from optically thick atomic transitions by analyzing the respective peak spectral radiance. The deviation of the line peak from a Planck function is used to extrapolate to the lower state population density of the respective transition. This extrapolation is based upon other measured population densities [16, 29]. **Each transition used has been checked for black body limiting by evaluating the criterion of Johnston et al.**

$$\exp(-n_{j,l}\sigma_\lambda \Delta z) < 0.1$$ (6)

with the absorption cross section σ_λ, the lower state population density $n_{j,l}$ and a characteristic length Δz [35]. Lower state number den-

sities of the respective transitions have either been measured with other methods or have been evaluated from a best Boltzmann-fit. The characteristic length needed to fulfill this criterion is a fraction of a millimetre for the transitions used. The optical path length of the spectroscopic system is in the order of $100\,\text{mm}$ [16]. Hence, black body limiting was confirmed for these transitions. The low energy and ground state population densities that have been determined by the black body limit or by the branching ratio discussed in section 2.4.2 are summed to yield the total number density of the respective atom.

2.4.4. Molecular Number Densities - Quasi Steady State Extrapolation (QSS)

Total number densities of molecular species are determined based on the absolute emitted radiation of electronically excited states [30, 36, 6]. **Collisional and radiative processes are accounted for in this analysis** [37, 38, 39, 40]. **The N_2^+ first negative system ($B^2\Sigma_u^+ \to X^2\Sigma_g^+$) and the N_2 second positive system ($C^3\Pi_u \to B^3\Pi_g$) are analysed.** A simulation of the emitted radiation of the respective molecule is conducted, using the non-Boltzmann model included in **NEQAIR 14.0** [41]. All other measured particle densities and temperatures are used as input for this radiative computation. Finally, the total species number densities of N_2 and N_2^+ are varied until the best agreement between the local emission coefficient of experiment and simulation is reached.

2.4.5. Electron and Ion Number Densities - Saha Extrapolation (SE)

Electron and ion densities are determined by applying a Saha equilibrium between highly excited atomic states and their respective ions [29]. The measured population densities of the excited atomic states are used to extrapolate to a virtual energy level at the ionization energy. The extrapolated population density is applied to the Saha equation in the formulation of van der Sijde and van der Mullen under the assumption of quasi-neutrality [42].

2.4.6. Electronic Excitation Temperature - Boltzmann Plot (BP)

The measured population densities of different excited atomic states are used to fit a Boltzmann relation where the electronic excitation temperature is varied until the best agreement between fitted function and measured states is achieved [31, 11, 42, 16].

2.4.7. Rotational and Vibrational Temperature - Molecular Band Shape (BS)

The local emission coefficient of electronic rovibrational molecular transitions of N_2 and N_2^+ is used to determine the rotational and vibrational **temperatures**. A simulation of the **emitted** radiation is conducted where these two excitation temperatures are varied until the best agreement between experiment and simulation is achieved [30, 43, 11, 44, 45, 46, 47]

2.4.8. Mass–specific Enthalpy (ME)

Local mass–specific enthalpy has been determined from spectroscopic measurements in past investigations [48, 49, 50, 9]. The extensive dataset of thermodynamic parameters derived by the spectroscopic measurements of this study and the measurements conducted by Zander et al. [17] allow**, for the first time,** the calculation of the local mass specific enthalpy of the non-equilibrium flow. The contributions of different modes of energy storage yield the total mass specific enthalpy via

$$h_0 = \overbrace{R \cdot T_{\mathrm{tr}}}^{h_{\text{volume change}}} + \overbrace{\frac{u_\infty^2}{2}}^{h_{\text{kinetic}}} + \overbrace{\sum_i^{\text{species}} \xi_i \cdot h_{\text{formation},\,i}}^{h_{\text{chemical}}} + \overbrace{\sum_i^{\text{species}} \xi_i \cdot \frac{3}{2} R_i \cdot T_{\mathrm{tr}}}^{h_{\text{thermal}}}$$

$$+ \underbrace{\sum_i^{\text{molecules}} \xi_i \cdot \frac{R_i \cdot \theta_{\text{vib},\,i}}{e^{\frac{\theta_{\text{vib},\,i}}{T_{\text{vib}}}} - 1}}_{h_{\text{vibrational}}} + \underbrace{\sum_i^{\text{molecules}} \xi_i \cdot R_i \cdot T_{\text{rot}}}_{h_{\text{rotational}}} + \underbrace{\sum_i^{\text{species}} \xi_i \cdot \frac{R_i \sum_j \theta_{\text{el},\,j} \cdot e^{\frac{-\theta_{\text{el},\,j}}{T_{\text{el}}}}}{Q_{\text{el}}}}_{h_{\text{electronic}}} \quad (7)$$

It is assumed that the gas consists of the measured species N, O, N_2, N_2^+, N^+, O^+ and e^-, as the number densities of the remaining species are negligibly small. **This allows the calculation of the respective mass fractions ξ_i and thus the calculation of the specific gas constant R from the single**

13

Table 2: Uncertainty sources for the different spectroscopic analysis methods.

	Particle or population densities					Temperatures		ME [h]
	EC [a]	BR [b]	BBL [c]	QSS [d]	SE [e]	BP [f]	BS [g]	
CCD chip [i] [53, 54, 55]	×	×	×	×			×	
A_{ul} [56]	×	×	×					
Calibration lamp	×		×	×			×	
Abel-transformation [57]	×			×			×	
Slit function		×	×				×	
Stark width [58]		×	×					
T_{el} (N, O)		×	×	×	×			×
T_{rot}		×	×	×				×
T_{vib}				×				×
n_j $(j = e^-)$		×	×	×				×
n_j $(j = N, O, N_2, N_2^+, N^+, O^+)$				×				×
$n_{j,i}$ $(j = N, O)$		×	×		×	×		

[a] Emission coefficient, [b] Branching ratio, [c] Black body limit extrapolation, [d] Quasi steady state extrapolation, [e] Saha extrapolation, [f] Boltzmann plot, [g] Molecular band shape, [h] Mass–specific enthalpy, [i] Thermal noise, shot noise, readout noise

specific gas constants R_i of each species [51]. The translational temperature and the flow velocity are taken from the work of Zander et al. [17]. The data of the heats of formation $h_{\mathrm{formation},i}$ is taken from the work of Grau [52]. The characteristic vibrational temperatures $\theta_{\mathrm{vib},i}$ are taken from the work of Vincenti and Krüger and the characteristic electronic temperatures $\theta_{\mathrm{el},j}$ and the electronic partition **functions** Q_{el} are taken from Park [51, 4].

2.4.9. Uncertainty analysis

The uncertainty analysis is conducted using the methodology of Moffat [59]. **The analysis method for the determination of the parameter P is applied multiple times. Each time a different input parameter X_i is altered by the respective uncertainty ΔX_i.** With this approach, the deviation from the nominal result $\partial P / \partial X_i \cdot \Delta X_i$ is calculated directly. The

determined deviations are then combined using

$$\Delta P = \sqrt{\sum_{i=1}^{N} \left(\frac{\partial P}{\partial X_i} \Delta X_i \right)^2} \tag{8}$$

and yield the total uncertainty ΔP of the respective analysis method. Different sources for the measurement uncertainty are identified and compiled in Table 2. **Here, the uncertainty sources which have been considered for the different analysis methods are shown.** The resulting uncertainty for the determined thermodynamic parameters is presented in Table 3.

Table 3: Uncertainties for the determined thermodynamic parameters.

Parameter	n_N	n_O	n_{N_2}	$n_{N_2^+}$	n_{N^+}	n_{O^+}	n_{e^-}	$T_{el, N}$	$T_{el, O}$	T_{rot}	T_{vib}	h_0
Uncertainty	25 %	45 %	176 %	40 %	28 %	38 %	26 %	7 %	12 %	9 %	11 %	7 %

3. Results

This section presents the resulting thermodynamic parameters along the stagnation line in front of the 80 mm diameter flat faced copper probe.

3.1. Particle Densities

The free stream parameters on the stagnation streamline 20 mm in front of the probe surface, i. e. at $x = 250$ mm, are summarized in Table 4. Additionally, an equilibrium chemical composition has been calculated corresponding to the measured static pressure and the measured mass-specific enthalpy using the *Chemical Equilibrium and Applications* program of Gordon and McBride [60]. Considering the typical 11 air species, as suggested by Park, the number densities of O_2, NO, O_2^+ and NO^+ are negligible and therefore not covered by the analysis of this work [61]. **It is clear from the measurements that the flowfield on the stagnation line is almost completely dissociated with only very few molecules remaining.**

Table 4: Particle densities on the stagnation streamline of the undisturbed flow at $x = 250\,\text{mm}$ from the nozzle exit.

Species	Measurement / m^{-3}	Equilibrium / m^{-3}
n_{tot}	$1.45 \pm 0.27 \cdot 10^{22}$	$1.18 \cdot 10^{22}$
n_{N}	$9.99 \pm 2.50 \cdot 10^{21}$	$5.89 \cdot 10^{21}$
n_{O}	$1.95 \pm 0.96 \cdot 10^{21}$	$1.72 \cdot 10^{21}$
n_{e^-}	$1.25 \pm 0.32 \cdot 10^{21}$	$2.09 \cdot 10^{21}$
n_{N^+}	$1.10 \pm 0.31 \cdot 10^{21}$	$1.75 \cdot 10^{21}$
n_{O^+}	$1.43 \pm 0.54 \cdot 10^{20}$	$3.29 \cdot 10^{20}$
n_{N_2}	$6.30 \pm 11.08 \cdot 10^{19}$	$2.05 \cdot 10^{17}$
$n_{\text{N}_2^+}$	$1.23 \pm 0.49 \cdot 10^{18}$	$4.24 \cdot 10^{16}$
n_{NO^+}	-	$8.06 \cdot 10^{16}$
n_{NO}	-	$7.90 \cdot 10^{15}$
$n_{\text{O}_2^+}$	-	$2.97 \cdot 10^{14}$
n_{O_2}	-	$1.52 \cdot 10^{14}$

The total number density of the measured flow is close to the equilibrium simulation while the composition exhibits some discrepancies from the equilibrium case. **The total number density agrees well with the equilibrium case as the translational temperature is close to the equilibrium value (see section 3.2). This follows from the ideal gas law**

$$p = n_{\text{tot}} k_B T_{\text{trans}} \tag{9}$$

where k_B is Boltzmann's constant. However, the chemical composition of the plasma shows a deviation from equilibrium which is discussed in the following. Considering the most abundant species, i. e. the atoms, oxygen is close to the equilibrium value while the nitrogen particle density is approximately 70 % higher in the plasma flow. **The atomic ions and electrons exhibit the opposite behaviour.** The number densities of these

16

species are between 57% and 37% below equilibrium. Interpretations of the N_2 measurement are not useful since the uncertainty is above 100%. The number density of N_2^+ is two **orders of** magnitude larger than the respective equilibrium value.

260 **The non-equilibrium state of the nitrogenous species could possibly be a result of the relatively short residence time in the electric arc. During that time the energy transfer into the gas is primarily established by collisions between nitrogen molecules and the electrons of the arc's electric current.** Thus, it is assumed that the two reactions

265

$$N_2 + e^- \rightarrow N_2^+ + e^- + e^- \tag{10}$$

and

$$N_2 + e^- \rightarrow N + N + e^- \tag{11}$$
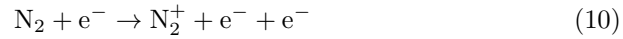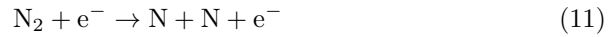
are the essential mechanisms of energy transfer. The main pathway for the production of N^+ particles in the electric arc is assumed to be the electron impact ionization reaction

$$N + e^- \rightarrow N^+ + e^- + e^-. \tag{12}$$

270 From the measured particle densities **it is possible** that the reactions (10) and (11) are the predominant mechanisms in the arc which would explain the higher than equilibrium values of $n_{N_2^+}$ and n_N. In contrast, the further ionization (12) of nitrogen atoms to N^+ does obviously not occur at a high enough rate which explains the relatively low value of n_{N^+}. This two step process of dissociation 275 and ionization takes too long to achieve an equilibrium composition. The measured non-equilibrium composition at $250\,\mathrm{mm}$ after the nozzle also clearly shows that the relaxation rate is slow compared to the time of flight of the **particles involved**.

The total nitrogenous species make up $85 \pm 21\%$ of all particles while oxygen 280 makes up $15 \pm 7\%$. The uncertainties are within the desired values of standard air (78% N and 21% O). Hence, the simulated air flow results in the correct
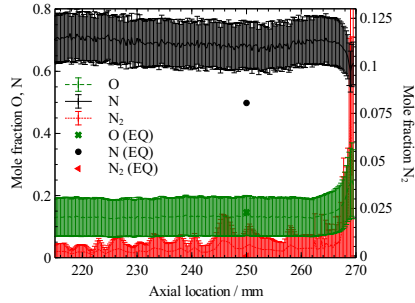
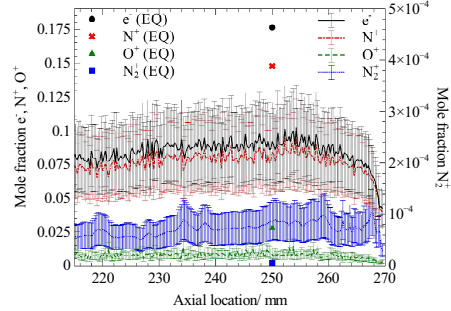Figure 6: Mole fraction distribution of neutral species on the stagnation streamline.

Figure 7: Mole fraction distribution of charged species on the stagnation streamline.

ratio between oxygen and nitrogen. This is not immediately clear since oxygen is **injected in** a nozzle segment **downstream of** the throat. Consequently, the two species have to mix in the nozzle and further downstream. The **energy**

285 **transfer** between oxygen and nitrogen particles during this mixing process **is** also the primary pathway for the excitation of oxygen atoms which was shown by high speed camera measurements [62]. This leads to the conclusion that the cold oxygen gas in the nozzle is heated less by the arc when compared to nitrogen. Thus, the arc's energy **transfer** seems to work best in the nozzle

290 throat which is consistent with classical arc-jet theory [63].

Figures 6 and 7 show the axial distribution of the mole fractions of the measured species (the probe surface is at 270 mm). As the axial gradient of the free stream is comparably small, the plasma exhibits characteristics of a frozen flow [1]. The nitrogen mole fraction slowly decreases towards its equilibrium

295 value. The oxygen mole fraction in the free stream remains completely frozen while an interpretation of the molecular nitrogen behavior is again not useful due to the large uncertainty. The mole fraction of the atomic ions in Fig. 7 exhibit a slight increase towards the equilibrium value.

The influence of the probe on the flow properties is first noticed through the

300 ion mole fractions 15 mm in front of the surface. In front of the boundary layer the atomic nitrogen mole fraction increases slightly since the dissociation degree

18

is elevated through the conversion of kinetic energy to **internal** energy. **The nitrogen atomic mole fraction rapidly decreases from 5 mm in front of the surface. The molecular nitrogen mole fraction consequently increases due to the recombination reactions occurring in the boundary layer and at the catalytic surface [64]. The probe surface is covered by oxidised copper which has been shown to be highly catalytic [65].** Interestingly, the atomic oxygen mole fraction increases towards the surface. As two nitrogen atoms recombine to one molecule, the mole fraction of the remaining oxygen atoms is increased. It is expected that significant oxygen recombination occurs closer to the surface, i. e. at lower boundary layer temperatures, when compared to nitrogen [11]. This is due to the lower dissociation energy of oxygen which results in a higher oxygen dissociation degree when compared to nitrogen. Thus, a smaller boundary layer thickness is expected for oxygen which might be below the resolution capability of the optical system. A further possible source for the oxygen behavior is a slip boundary condition at the wall which has also been observed in the numerical simulation of the flight at this trajectory point [15].

The mole fraction of atomic ions decreases towards the surface from approximately $x = 260\,\mathrm{mm}$. The N_2^+ mole fraction decreases from only $2\,\mathrm{mm}$ in front of the surface. This might be a result of the increased charge exchange reaction

$$N_2 + N^+ \rightarrow N_2^+ + N \tag{13}$$

which is elevated due to the more abundant nitrogen molecules in the boundary layer [30, 52]. The electron density measured by Zander et al. using **Fabry-Perot** interferometry is $44\,\%$ below the value determined in this work while the uncertainty margins of both methods barely overlap. The discrepancy might be a result of a deviation from the Saha-equilibrium or from quasineutrality in the flow.

19

Table 5: Temperatures on the stagnation streamline of the undisturbed flow at $x = 250\,\mathrm{mm}$ from the nozzle exit.

Temperature	Measurement / K	Equilibrium / K
$T_{\mathrm{el,\,N}}$	9490 ± 670	
$T_{\mathrm{el,\,O}}$	11000 ± 1320	
T_{vib}	12370 ± 1360	
T_{rot}	10980 ± 990	10170
$T_{\mathrm{trans,\,N}}$ [66]	11000 ± 1200	
$T_{\mathrm{trans,\,O}}$ [66]	13500 ± 2000	
$T_{\mathrm{trans,\,mean}}$	11530 ± 1040	

3.2. Excitation Temperatures

330   The measured and equilibrium values of the excitation temperatures on the stagnation streamline at $x = 250\,\mathrm{mm}$ are summarized in Table 5. Additionally, the translational temperatures of atomic nitrogen and oxygen measured by Zander et al. are compiled in the table [66]. The mean translational temperature is determined by a mole fraction averaging of the two measured atomic transla-

335   tional temperatures [6]. All measured temperatures are above the equilibrium temperature except for the electronic excitation temperature of atomic nitrogen. **The higher than equilibrium temperatures correspond to a typical situation of a relaxation region behind a hypersonic shock wave, i. e. the flow field region which the plasma wind tunnel is attempting**

340   **to reproduce [20]. The rather high vibrational temperature might be a result of a non-Boltzmann distribution of vibrational states which occurs due to preferential dissociation effects [18, 67].** It is also noted that the often assumed equilibrium between mean translational and rotational temperature holds true.

345   Figure 8 shows the axial distribution of the electronic excitation temperatures of atomic oxygen and nitrogen along the stagnation streamline. Both
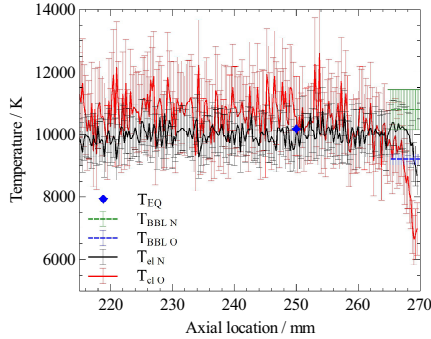
20

Figure 8: Electronic excitation temperature distribution on the stagnation streamline [16].
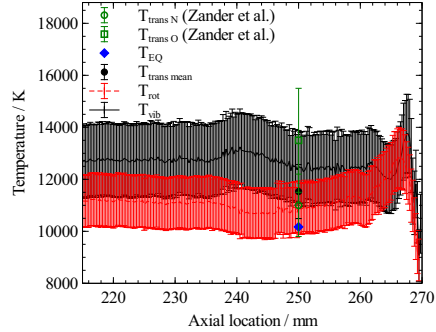

Figure 9: Molecular excitation temperature distribution on the stagnation streamline [66].

temperatures are essentially constant at the equilibrium temperature over the complete free stream region. **The figure also includes black body limit temperatures measured from stagnation point VUV spectra which apply to the first few millimeters in front of the probe [16].** Therefore, these temperatures are plotted as constant within this region. The two black body limit temperatures **agree with** the different boundary layer temperatures of the two atoms, which have been obtained with the Boltzmann-plot method described in section 2.4.6.

Figure 9 shows the distribution of the molecular excitation temperatures on the stagnation streamline. **Both temperatures remain constant** except for a slight disturbance at 245 mm. The probe results in an increase of the rotational temperature which is expected from a compressing flow. **The** kinetic energy of the flow is transferred to rotational and translational degrees of freedom [68]. At 5 mm from the surface the rotational temperature begins to decrease towards the surface temperature. The vibrational temperature, however, shows a peculiar **behaviour**. At 5 mm in front of the surface it exhibits a local minimum and a maximum at 2 mm from the surface before the expected boundary layer temperature decrease occurs. **Due to the flow compression**

21

Table 6: Mass–specific enthalpy on the stagnation streamline.

	Spectroscopic measurement	p_tot, $\dot{q}$ **probe**	**Mass-injection** probe
h_0 / $\mathrm{MJ\,kg^{-1}}$	62.3 ± 4.5	76.4 ± 22.9	70.1 ± 21.0

more collisions lead to a more rapid relaxation towards the translational/rotational temperature which explains the decrease at 5 mm from the surface. After the two curves cross the vibrational temperature follows the rotational temperature due to the relaxation of vibration towards translation/rotation. The increase near the surface might be caused by exchange reactions resulting in vibrationally highly excited molecules which lead to an elevated apparent vibrational temperature.

3.3. Mass–specific Enthalpy

Table 6 presents the different measurements of the mass–specific enthalpy on the stagnation streamline in front of the probe. The spectroscopic measurement, as described in section 2.4.8, is compared to the two values obtained with the probe measurements described in sections 2.1 and 2.2. **The agreement between the results of the three vastly different measurement approaches is good. The measured values of the mass-injection probe and spectroscopy are 17 % and 6 % below the value measured with the heat flux and stagnation pressure probe. This deviation is within the expected uncertainties of the probe measurements. These are assumed to be 30 %.** In the following, the composition of the enthalpy is studied further.

Table 7 summarizes the contributions from different energy modes to the static enthalpy at $x = 250\,\mathrm{mm}$, as described by Eq. (7). The measured enthalpy is essentially a combination of thermal, chemical and volume change contribu-

22

Table 7: Relative contributions to the static enthalpy on the stagnation streamline of the undisturbed flow at $x = 250\,\mathrm{mm}$ from the nozzle exit.

Enthalpy mode	Measurement / %	Equilibrium / %
Chemical	64.0 ± 3.9	71.2
Thermal	19.3 ± 1.4	15.4
Volume change	12.9 ± 1.1	10.5
Electronic	3.8 ± 0.5	2.9
Rotational	$5.9 \pm 5.9 \cdot 10^{-2}$	$3.1 \cdot 10^{-4}$
Vibrational	$5.1 \pm 5.1 \cdot 10^{-2}$	$1.6 \cdot 10^{-4}$

tions. The remaining energy in the excitation of internal modes is negligibly small. In particular, vibrational and rotational energies are very small since **the flow is mostly** dissociated. As all particles are able to be electronically excited, this mode contains more energy. The comparison between simulation and measurement reveals that the equilibrium value is outside the uncertainty margin of each mode, except the molecular excitation modes. However, due to the large uncertainty and their insignificance an interpretation of these values is not useful. **The higher than equilibrium translational temperature** results in an elevated energy stored in the thermal and volume change modes while the relatively small amount of **ionisation** is mainly responsible for the low energy stored in the chemical composition. The energy stored in electronic modes is higher than equilibrium due to the comparatively large amount of atomic nitrogen. The splitting of metastable low energy states results in more excited particles compared to oxygen. Thus, with more nitrogen atoms more enthalpy is stored in electronically excited states.

4. Conclusion

This work presents results from emission spectroscopic and probe measurement of an arc-jet plasma wind tunnel flow corresponding

23

to the Hayabusa re-entry trajectory point at 78.8 km altitude. Heat flux and total pressure have been measured with an 80 mm diameter flat faced cylindrical probe. Local mass specific enthalpy has been determined from these values using standard correlation methods with measured velocity gradients in front of different geometries. Additionally, an enthalpy probe is employed where the local mass–specific enthalpy is determined from a heat flux reduction due to mass injection at the stagnation point. Spectroscopic measurements are employed in the UV-NIR spectral regime capturing the spatially resolved radiation along the stagnation line of the flowfield in front of an 80 mm diameter flat faced probe. Multiple diagnostic methods are used to deduce the absolute number densities of N_2, N_2^+, N, O, N^+, O^+ and e^- and the temperatures of electronic, vibrational and rotational excitation. A detailed uncertainty analysis is conducted considering multiple sources of uncertainty for each method. The measured thermodynamic properties are used to calculate the local mass–specific enthalpy of the non-equilibrium flow.

This work provides a comprehensive assessment of the thermochemical flowfield parameters of a subsonic high enthalpy plasma flow corresponding to a superorbital re-entry flow condition. The flowfield features properties of a frozen flow with a distinct non-equilibrium of nitrogenous species which is assumed to be a result of a short exposure of the cold gas to the electric arc. This is also a reason for the lower than equilibrium mole fraction of atomic ions and electrons. The boundary layer thickness differs greatly between different species and features significantly less nitrogen atoms than oxygen atoms due to a higher rate of nitrogen recombination reactions. Excitation temperatures of electronic, vibrational and rotational modes show constant behavior in the free stream while the boundary layer profile differs greatly between the various excitation temperatures.

The spectroscopically determined local mass-specific enthalpy is in **good** agreement with the two probe based measurements. The flow exhibits a thermal energy content higher than equilibrium and a correspondingly lower chemical energy component. However, the deviation from equilibrium is small. This

24

situation is similar to **a near equilibrium point** behind a hypersonic shock wave, i. e. the aim of the reproduction of this regime is shown to be successful.

Acknowledgments

References

[1] J. D. Anderson, Hypersonic and High-Temperature Gas Dynamics, 2nd Edition, 2nd Edition, AIAA Education Series, 2006.

[2] P. A. Gnoffo, Planetary-entry gas dynamics, Annual Review of Fluid Mechanics 31 (1999) 459–494. `doi:10.1146/annurev.fluid.31.1.459`. URL `http://arjournals.annualreviews.org/doi/full/10.1146/annurev.fluid.31.1.459`

[3] F. K. Lu, D. E. Marren (Eds.), Advanced Hypersonic Test Facilities, Vol. 198 of Progress in Astronautics and Aeronautics, AIAA, 2002, iSBN 1-56347-541-3.

[4] C. Park, Nonequilibrium Hypersonic Aerothermodynamics, John Wiley & Sons, 1990.

[5] S. Loehle, T. Hermann, F. Zander, Experimental assessment of the performance of ablative heat shield materials from plasma wind tunnel testing, in: 8th ESA Workshop on Thermal Protection Systems and Hot Structures, ESA, 2016.

[6] T. Hermann, S. Loehle, S. Fasoulas, P. Leyland, L. Marraffa, J.-M. Bouilly, Influence of ablation on vacuum-ultraviolet radiation in a plasma wind tunnel flow, Journal of Thermophysics and Heat TransferAccepted.

[7] S. Loehle, S. Fasoulas, G. Herdrich, T. Hermann, B. Massuti-Ballester, A. Meindl, A. S. Pagan, F. Zander, The plasma wind tunnels at the institute of space systems: Current status and challenges, in: 46th Aerodynamic Measurement Technology and Ground Testing Conference, AIAA, 2016.

[8] A. F. Kolesnikov, Extrapolation from high enthalpy tests to flight based on the concept of local heat transfer simulatinon, in: Measurement Techniques for High Enthalpy and Plasma Flows, no. 8B, VKI, RTO — Research and Technology Organization, Rhode–Saint–Genese, Belgium, 1999.

[9] S. Löhle, Untersuchung von wiedereintrittsplasmen mit hilfe laserinduzierter fluoreszenzmessungen, Dissertation, Universität Stuttgart, Institut für Raumfahrsysteme (2006).

[10] T. Marynowski, S. Loehle, S. Fasoulas, F. Zander, A. Meindl, Aerothermodynamic investigation of inductively heated co2 plasma flows for mars entry testing, in: 45th AIAA Plasmadynamics and Lasers Conference, AIAA Aviation, American Institute of Aeronautics and Astronautics, 2014. doi:10.2514/6.2014-2537.

[11] M. W. Winter, Emissionsspektroskopische untersuchung der umströmung von probenkörpern in hochenthalpen plasmaströmungen, Ph.D. thesis, Institut für Raumfahrtsysteme, Stuttgart (2007).

[12] W. Röck, Simulation des eintritts einer sonde in die atmosphäre des saturn-mondes titan in einem plasmawindkanal, Ph.D. thesis, Institut für Raumfahrtsysteme, Universität Stuttgart, Germany, (in German) (1999).

[13] C. O. Laux, R. J. Gessman, C. H. Kruger, F. Roux, F. Michaud, S. P. Davis, Rotational temperature measurements in air and nitrogen

26

plasmas using the first negative system of n2+, Journal of Quantitative Spectroscopy and Radiative Transfer 68 (4) (2001) 473 – 482. `doi:10.1016/s0022-4073(00)00083-2`.

URL `http://www.sciencedirect.com/science/article/pii/S0022407300000832`

[14] D. G. Fletcher, M. Playez, Characterization of supersonic and subsonic plasma flows, in: 25th AIAA Aerodynamic Measurement Technology and Ground Testing Conference, San Francisco, California, 2006. `doi:10.2514/6.2006-3294`.

[15] S. Löhle, A. Brandis, T. Hermann, J. Peter, Numerical investigation of the re-entry flight of hayabusa and comparison to flight and ground testing data, in: 43rd AIAA Thermophysics Conference, AIAA, New Orleans, LA, 2012.

[16] T. Hermann, S. Löhle, F. Zander, H. Fulge, S. Fasoulas, Characterization of a re-entry plasma wind tunnel flow with vacuum ultraviolet to near infrared spectroscopy, Journal of Thermophysics and Heat Transfer 30 (3) (2016) 673–688, accepted for publication. `doi:http://arc.aiaa.org/doi/abs/10.2514/1.T4695`.

[17] F. Zander, S. Loehle, Analysis of air plasma flows in magnetoplasmadynamic arcjet testing, in: 46th AIAA Thermophysics Conference, Washington, DC, 2016.

[18] S. Loehle, T. Hermann, F. Zander, T. Marynowski, Echelle spectroscopy for high enthalpy flow diagnostics, in: 46th Aerodynamic Measurement Technology and Ground Testing Conference, AIAA, 2016.

[19] M. Auweter-Kurtz, H. Kurtz, S. Laure, Plasma generators for re-entry simulation, Journal of Propulsion and Power 12 (6) (1996) 1053–1061.

[20] S. Laure, Experimentelle simulation der staupunktströmung wiedereintretender raumflugkörper und deren charakterisierung mittels mechanischer

27

sonden, Dissertation, Universität Stuttgart, Institut für Raumfahrtsysteme
(1998).

[21] S. Loehle, A. Steinbeck, S. Fasoulas, Local mass-specific enthalpy measurements with a new mass injection probe, Jornal of Thermophysics and Heat Transferdoi:10.2514/1.t4709.

[22] S. Fasoulas, T. Stöckle, M. Auweter-Kurtz, Measurement of specific enthalpy in plasma wind tunnels using a mass injection probe, in: 32nd AIAA Thermophysics Conference, no. AIAA 1997-2496, AIAA, Atlanta, GA, 1997.

[23] R. Wernitz, C. Eichhorn, G. Herdrich, S. Löhle, S. Fasoulas, H.-P. Röser, Plasma wind tunnel investigation of european ablators in air using emission spectroscopy, in: 42nd AIAA Thermophysics Conference, 2011.

[24] Standard test method for calculation of stagnation enthalpy from heat transfer theory and experimental measurements of stagnation-point heat transfer and pressure (e 637-05), Tech. rep., ASTM (2005).

[25] E. V. Zoby, Empirical stagnation-point heat-transfer relation in several gas mixtures at high enthalpy levels, NASA Technical Note (TN D-4799).

[26] I. Sakraker, A. Turchi, O. Chazot, Hypersonic aerothermochemistry duplication in ground plasma facilities: A flight-to-ground approach, Journal of Spacecraft and Rocketsdoi:10.2514/1.A33137.

[27] R. D. Brown, A comparison of the theoretical and experimental stagnation-point heat transfer in an arc-heated subsonic stream, Tech. Rep. NASA TN D-1927, NASA Langley Research Center (1964).

[28] H. Fulge, S. Löhle, S. Fasoulas, A noise resistant abel transformation algorithm tested on optical emission spectroscopy, Jornal of Thermophysics and Heat Transfer 30 (2) (2016) 266–273. doi:10.2514/1.T4802.

28

[29] T. Hermann, S. Löhle, H. Wei, R. Morgan, U. Bauder, S. Fasoulas, Quantitative emission spectroscopy for superorbital re-entry in the expansion tube x2, AIAA Journal of Thermophysics and Heat TransferAccepted. `doi:10.2514/1.T4898`.

[30] C. O. Laux, Optical diagnostics and radiative emission of air plasmas, Ph.D. thesis, Stanford University (1993).

[31] D. G. Fletcher, Nonintrusive diagnostic strategies for arcjet stream characterization, Vol. Measurement Techniques for High Enthalpy and Plasma Flows, 1999.

[32] R. Stirn, Emissionsspektroskopische untersuchungen der wechselwirkung eines freistrahls mit hitzeschutzmaterialien, Ph.D. thesis, Institut für Plasmaforschung der Universität Stuttgart (Dec. 2005).

[33] G. Laity, A. Fierro, J. Dickens, A. Neuber, K. Frank, Simultaneous measurement of nitrogen and hydrogen dissociation from vacuum ultraviolet self-absorption spectroscopy in a developing low temperature plasma at atmospheric pressure, Applied Physics Letters 102 (184104). `doi: 10.1063/1.4804369`.

[34] J. B. Boffard, R. O. Jung, C. C. Lin, A. E. Wendt, Measurement of metastable and resonance level densities in rare-gas plasmas by optical emission spectroscopy, Plasma Sources Science and Technology 18 (2009) 1–11.

[35] C. O. Johnston, A. M. Brandis, Features of afterbody radiative heating for earth entry, in: 11th AIAA/ASME Joint Thermophysics and Heat Transfer Conference, Atlanta, GA, 2014.

[36] S. Löhle, S. Lein, C. Eichhorn, G. Herdrich, M. W. Winter, Spectroscopic investigation of an inductively heated co2 plasma for mars entry simulation, Journal of Technical Physics.

[37] K. Kano, M. Suzuki, H. Akatsuka, Spectroscopic measurement of electron temperature and density in argon plasmas based on collisional-radiative model, Plasma Sources Sci. Technol. 9 (3). `doi:10.1088/0963-0252/9/3/309`.

[38] A. Fierro, G. Laity, A. Neuber, Optical emission spectroscopy study in the vuv-vis regimes of a developing low-temperature plasma in nitrogen gas, Journal of Physics D: Applied Physics 45 (49). `doi:10.1088/0022-3727/45/49/495202`.

[39] S. Keller, P. Rajasekaran, N. Bibinov, P. Awakowicz, Characterization of transient discharges under atmospheric-pressure conditions applying nitrogen photoemission and current measurements, Journal of Physics D: Applied Physics 45 (12) (2012) 125202.
URL `http://stacks.iop.org/0022-3727/45/i=12/a=125202`

[40] S. D. Popa, Influence of pressure on spectral intensities in a flowing nitrogen glow discharge, Journal of Physics D: Applied Physics 29 (2) (1996) 416–418. `doi:10.1088/0022-3727/29/2/019`.

[41] C. Park, Convergence of computation of chemical reacting flows, Progress in Astronautics and Aeronautics 103 (1986) 478–513.

[42] B. van der Sijde, J. A. M. van der Mullen, Temperature determination in non-lte plasmas, Journal of Quantitative Spectroscopy and Radiative Tranfer 44 (1) (1990) 39–46.

[43] D. G. Fletcher, Nonintrusive diagnostic strategies for arcjet stream chracterization, in: Measurement Techniques for High Enthalpy and Plasma Flows, VKI, RTO — Research and Technology Organization, Rhode–Saint–Genese, Belgium, 1999.

[44] S. Löhle, S. Lein, C. Eichhorn, G. Herdrich, M. Winter, Spectroscopic investigation of an inductively heated co2 plasma for mars entry simulation, Journal of Technical Physics 50 (3) (2009) 151–164.

30

[45] C. O. Laux, M. Winter, J. A. Merrifield, A. Smith, P. Tran, Influence of ablation products on the radiation at the surface of a blunt hypersonic vehicle at 10 km/s, in: 41st AIAA Thermophysics Conference, no. AIAA 2009-3925, 2009.

[46] T. Eichmann, Radiation measurements in a simulated mars atmosphere, Ph.D. thesis, University of Queensland (2012).

[47] B. Kraetzig, S. Löhle, D. Buttsworth, Evolution of plasma species and heat-shield temperatures from hayabusa reentry observation, AIAA Journal of Spacecrafts and Rockets 51 (3). `doi:10.2514/1.A32854`.

[48] D. Babikian, C. Park, G. Raiche, Spectroscopic determination of enthalpy in an arc-jet wind tunnel, in: 33rd Aerospace Sciences Meeting and Exhibit, American Institute of Aeronautics and Astronautics, 1995. `doi:10.2514/6.1995-712`.

[49] S. Lein, Entwicklung eines auf emissionsspektroskopie basierenden sensorsystems zum einsatz auf wiedereintrittsplattformen, Ph.D. thesis, Universität Stuttgart, to be published (2012).

[50] C. Park, G. A. Raiche, D. M. Driver, J. Olejniczak, Comparison of enthalpy determination methods for arc-jet facility, AIAA Journal of Thermophyiscs and Heat Transfer 20 (4) (2006) 672–679.

[51] W. G. Vincenti, C. H. Kruger, Introduction to Physical Gas Dynamics, John Wiley & Sons, New York, 1965.

[52] T. Grau, Numerische untersuchung von plasmawindkanalströmungen zur wiedereintrittssimulation, Ph.D. thesis, Institut für Raumfahrtsysteme, Universität Stuttgart (2000).

[53] A. Thorne, U. Litzén, S. Johansson, Spectrophysics: Principles and Applications, Springer, 1999.

31

[54] L. Mortara, A. Fowler, Evaluations of charge-coupled device (ccd) performance for astronomical use, Solid-State Imagers for Astronomy 290 (28).

[55] S. B. Howell, Handbook of CCD Astronomy, Cambridge University Press, 2000.

[56] National Institute of Standards and Technology, http://physics.nist.gov/PhysRefData/ASD (2014).
URL http://www.nist.gov

[57] H. Fulge, A. Knapp, C. Eichhorn, R. Wernitz, S. Loehle, S. Fasoulas, G. Herdrich, Improved abel inversion method for analysis of spectral and photo-optical data of magnetic influenced plasma flows, 42nd AIAA Plasmadynamics and Lasers Conference.

[58] C. O. Johnston, B. R. Hollis, K. Sutton, Spectrum modeling for air shock-layer radiation at lunar-return conditions, Journal of Spacecraft and Rockets 45 (5) (2008) 865–878.

[59] R. J. Moffat, Describing the uncertainties in experimental results, Experimental Thermal and Fluid Science 1 (1) (1988) 3 – 17. doi:10.1016/0894-1777(88)90043-x.
URL http://www.sciencedirect.com/science/article/pii/089417778890043X

[60] S. Gordon, B. J. McBride, Computer program for calculation of complex chemical equilibrium compositions and applications, Reference Publication 1311, NASA (1996).

[61] C. Park, Assessment of two-temperature kinetic model for ionizing air, Journal of Thermophysics and Heat Transfer 3 (1989) 233–244.

[62] F. Zander, T. Hermann, S. Loehle, Plasma wind tunnel flow analysis with high speed imaging, in: 46th AIAA Thermophysics Conference, 2016.

[63] M. Auweter-Kurtz, Zur dynamik der mit kaltgas angeströmten lichtbogensäule, Ph.D. thesis, Universität Stuttgart (1985).

[64] T. Stöckle, Untersuchung der oberflächenkatalyzität metallischer und keramischer werkstoffe in hochenthalpieströmungen, Dissertation, Universität Stuttgart, Institut für Raumfahrsysteme (2000).

[65] A. Steinbeck, M. Fertig, G. Herdrich, H.-P. Röser, Enhanced evaluation of recombination coefficient measurements in plasma wind tunnels, AIAA-Paper 2009-3933, 41st AIAA Thermophysics Conference, San Antonio, Texas (Jun. 2009).

[66] F. Zander, S. Löhle, T. Hermann, A parametric study of the rd5 magnetoplasmadynamic generator using high resolution spectroscopy, in: 7th International Workshop on Radiation of High Temperature Gases, 2016.

[67] T. Hermann, S. Löhle, S. Fasoulas, A. Andrianatos, Tomographic optical emission spectroscopy for plasma wind tunnel testing, Applied OpticsUnder review.

[68] D. Potter, Modelling of radiating shock layers for atmospheric entry at earth and mars, Ph.D. thesis, The University of Queensland, St. Lucia, Australia (May 2011).